

# Measurement of the $6d^2D_J$ hyperfine structure of cesium using resonant two-photon sub-Doppler spectroscopy

A. Kortyna, N. A. Masluk,\* and T. Bragdon†

*Department of Physics, Lafayette College, Easton, Pennsylvania 18042, USA*

(Received 14 February 2006; published 3 August 2006)

We report the hyperfine coupling constants for the  $6d^2D_J$  states of  $^{133}\text{Cs}$  using two-color absorption spectroscopy with sub-Doppler resolution. Two single-mode diode lasers resonantly excite cesium in a low-pressure vapor cell. The frequency scale is directly referenced to the ground hyperfine interval of  $^{87}\text{Rb}$  using a radio-frequency modulation technique. The  $6d^2D_{5/2}$  coupling constants are measured as  $A=-4.66\pm 0.04$  MHz and  $B=0.9\pm 0.8$  MHz, agreeing with the literature. The  $6d^2D_{3/2}$  coupling constants are measured as  $A=16.34\pm 0.03$  MHz and  $B=-0.1\pm 0.2$  MHz, which significantly improve the precision of previous measurements.

DOI: [10.1103/PhysRevA.74.022503](https://doi.org/10.1103/PhysRevA.74.022503)

PACS number(s): 32.30.Bv

## I. INTRODUCTION

The hyperfine structures of alkali-metal atoms have long been a subject of considerable attention, as the 1977 comprehensive review by Arimondo *et al.* [1] indicates. More recently there has been renewed interest in alkali-metal hyperfine structures, including cesium's structures [2–7]. The high precision attained by a number of these measurements, especially that of Ref. [7], attest to the growing technical importance of cesium. Experimental considerations restrict the highest precision work to the  $s$  and  $p$  states, where agreement with theory is good [8]. On the other hand,  $d$ -state hyperfine structures remain a significant computational challenge because of strong correlation effects [9]. The  $d$  states of cesium are, therefore, well suited for testing the computational treatment of correlation, and their relatively narrow natural linewidths facilitate high resolution measurements. We report on the hyperfine splittings and the hyperfine coupling constants for the  $6d^2D_{5/2}$  and  $6d^2D_{3/2}$  states of atomic cesium, and we significantly improve the precision for the hyperfine coupling constants of the latter state.

Hyperfine interactions are sensitive to the details of nuclear structure, as well as to electron correlation effects, relativistic effects, and core polarization effects. An important motivation for our work is providing data for testing structure calculations needed to analyze recent parity non-conservation (PNC) measurements. PNC measurements include the work of Wood *et al.* [10] and Guéna *et al.* [11], both measuring the  $6s^2S_{1/2}\rightarrow 7s^2S_{1/2}$  dipole-forbidden transition amplitudes to high precision. Interpretation of these experiments requires calculating weak-interaction matrix elements. These matrix elements are sensitive to the details of the nuclear structure and to the overlap of the electronic wave function with the nucleus. The uncertainties associated with the deformed odd- $Z$  nature of the  $^{133}\text{Cs}$  nucleus—whose structure has not been accurately measured—make precise

*ab initio* calculations of the weak matrix elements difficult. Hyperfine coupling constants, however, provide insight into the interaction between the electrons and the nucleus, and the  $d$ -state hyperfine structure is sensitive to the nonzero radial distribution of nucleons. Hyperfine coupling constants can be measured highly accurately, making them good benchmarks for gauging the accuracy of PNC amplitude calculations. Performing such benchmarking is becoming increasingly common [12,13].

Finite nuclear effects have been studied computationally by Pollock and Welliver [14,15]. They point out that considerable uncertainties in cesium's neutron distribution lead to ambiguities in the degree to which  $p$ - $d$  effects mix into  $s$ - $s$  PNC amplitudes. However, they estimate that finite nuclear effects will probably become significant only after uncertainties in atomic theory calculations are further reduced.

A thorough understanding of the  $d$ -state hyperfine structure would also be important for interpreting proposed PNC measurements of  $ns^2S_{1/2}\rightarrow n'd^2D_{3/2}$  dipole-forbidden transitions [16]. Preliminary calculations by Dzuba *et al.* [9] suggest that  $ns^2S_{1/2}\rightarrow n'd^2D_{3/2}$  weak-interaction amplitudes may be four-times greater than corresponding  $ns^2S_{1/2}\rightarrow n's^2S_{1/2}$  amplitudes, but they encountered difficulties performing *ab initio* calculations because of strong  $d$ -state correlation effects. Sahoo *et al.* [13] show that it is critically important to consider correlation when using hyperfine coupling constants to estimate the accuracy of  $np^2P_{1/2}-6d^2D_{3/2}$  weak matrix elements, which are needed for  $ns^2S_{1/2}-n'd^2D_{3/2}$  PNC amplitudes calculations. Our results significantly reduce the uncertainties associated with the  $6d^2D_{3/2}$  hyperfine coupling constants, potentially improving theorists' ability to estimate the accuracy of their  $np^2P_{1/2}-6d^2D_{3/2}$  weak matrix element computations.

Beyond estimating the accuracy of weak matrix elements, work continues on reducing the contribution of atomic structure calculations to the overall uncertainty of the PNC analysis. For example, Safronova and Clark [17] compute electric dipole matrix elements for  $6p$ - $nd$  transitions of cesium (where  $n=5, 6,$  and  $7$ ), and use these matrix elements to determine polarizabilities and lifetimes. They find good agreement with experimental values of the scalar polarizability of the  $6p$  state, but poor agreement with  $5d$  lifetime mea-

\*Present address: Physics Department, Yale University, P.O. Box 20812, New Haven, CT 06520, USA.

†Present address: Physics Department, University of Connecticut, Storrs, CT 06269, USA.

measurements. This suggests that the polarizability measurements are incompatible with the lifetime measurements. They call for measuring additional  $d$ -states properties of atomic cesium to uncover the source of this inconsistency.

The hyperfine interaction energy [18]

$$W = \frac{1}{2}AK + \frac{1}{4}B \frac{3K(K+1)/2 - 2I(I+1)J(J-1)}{I(2I-1)J(2J-1)} \quad (1)$$

is dominated by two electromagnetic multipole terms, namely, the magnetic dipole moment and the electric quadrupole moment. Here,  $A$  and  $B$  are the magnetic dipole and electric quadrupole coupling constants,  $I$  is the nuclear angular momentum quantum number,  $J$  is the total electronic angular momentum quantum number,  $K = F(F+1) - J(J+1) - I(I+1)$ , and  $F$  is the total atomic angular momentum quantum number.

In this paper, we report our measurements of the hyperfine splittings and the resulting hyperfine coupling constants,  $A$  and  $B$ , for the  $6d^2D_{5/2}$  and  $6d^2D_{3/2}$  states of atomic cesium. We use two single-mode diode lasers to achieve sub-Doppler resolution with resonant two-photon absorption spectroscopy. We developed a radio frequency (RF) technique that directly references the hyperfine interval measurements to the precisely known ground hyperfine interval of atomic rubidium. This calibration technique provides stability and precision without the exacting mechanical and thermal requirements associated with many calibration methods. Our results agree with laser-spectroscopic measurements made previously for the  $6d^2D_{5/2}$  state in an ultracold trapped measurement [3]. In addition, we significantly improve upon the precision of the  $6d^2D_{3/2}$  hyperfine constants last measured using cascade fluorescence spectroscopy [19].

## II. EXPERIMENT

The ground state of cesium is not directly coupled to the  $nd$  states via electric-dipole radiation; we use two single-mode, external-cavity diode lasers to reach the  $6d^2D_J$  states via two-color resonant excitation, as illustrated in Fig. 1. The optical components of the absorption-spectroscopy apparatus (Fig. 2) are mounted on a pneumatically isolated optical table. The diode lasers use Littrow external cavities [20], where optical feedback from a diffraction grating improves frequency stability and tunability. Active temperature control reduces the frequency drift below 0.05 MHz/s, which is sufficiently small to ignore during data collection.

The first external cavity diode laser, labeled DL1 in Fig. 2, is fitted with a QPhotonics Corp. QLD-850-100S quantum-well laser diode. DL1 is tuned to either 852.335 nm for  $6s^2S_{1/2}(F=3) \rightarrow 6p^2P_{3/2}(F'=2,3,4)$  transitions, or 852.356 nm for  $6s^2S_{1/2}(F=4) \rightarrow 6p^2P_{3/2}(F'=3,4,5)$  transitions. DL1 is frequency locked to a saturated absorption signal using a servo-feedback circuit (see [20] for details on saturated absorption spectroscopy and frequency locking). We lock DL1 to one of several crossover peaks and shift the frequency to a zero-velocity resonance using a 75–150 MHz acousto-optic modulator (AMO) (IntraAction Corp., model ATM-1201A2). The AMO also modulates the laser beam

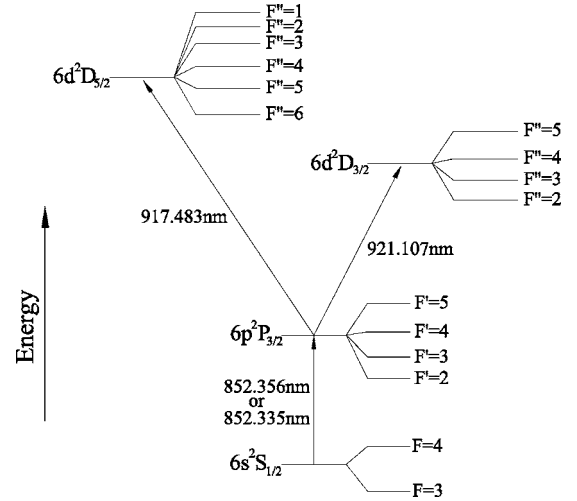


FIG. 1. The relevant energy levels and excitation scheme for  $^{133}\text{Cs}$ . The energy axis is not to scale and the wavelengths are vacuum values. Note the inverted  $6d^2D_{5/2}$  hyperfine structure.

amplitude at 15–30 kHz for phase-sensitive signal acquisition.

The second external cavity (DL2) is fitted with a QPhotonics Corp. QLD-920-100S laser diode and tuned to either 917.483 nm for  $6p^2P_{3/2}(F') \rightarrow 6d^2D_{5/2}(F'')$  transitions or 921.107 nm for  $6p^2P_{3/2}(F') \rightarrow 6d^2D_{3/2}(F'')$  transitions. The total atomic angular momentum quantum number of the target  $d$ -state,  $F''$ , ranges over  $2, \dots, 5$  for  $J = \frac{3}{2}$  and  $1, \dots, 6$  for  $J = \frac{5}{2}$ . By using various values of  $F'$  in the intermediate  $6p^2P_{3/2}$  state, this excitation scheme can access all  $F''$  sub-levels of both  $6d^2D_J$  manifolds. DL2 is scanned across the relevant hyperfine structure at rates of 20–100 MHz/s (for total scans of length 100–500 MHz). An electro-optic modulator (EOM) (New Focus Inc., model 4002) phase modulates the DL2 beam at 30–190 MHz to produce frequency cali-

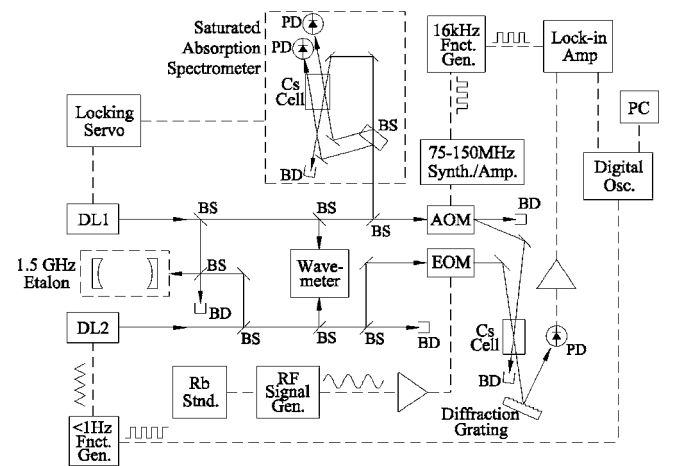


FIG. 2. Schematic of the experimental apparatus; DL1, diode laser 1; DL2, diode laser 2; BS, beam splitter; BD, beam dump; PD, photodiode; AOM, acousto-optic modulator; EOM, electro-optic modulator; Rb Stnd, atomic rubidium frequency standard; PC, desktop computer, broken lines, electrical signals; solid lines with arrows, laser beam paths.

bration markers (see Sec. II B for details on frequency calibration).

The two laser beams intersect at the center of a 10 cm long low-pressure Pyrex cesium vapor cell. After passing through the cell, DL1 enters a beam dump and DL2 strikes a 1200 line/mm diffraction grating. The first-order interference fringe illuminates a photodiode (PD), and the absorption signal is recovered through phase-sensitive detection by a lock-in amplifier (SRS, model SR510). The time constant of the detection circuit is 3 ms, and the absorption signal is digitized at a rate of 2 ms per point; a typical 15 MHz wide absorption peak is therefore traversed in 50–250 time constants and contains between 75 and 380 points. The DL2 frequency is alternately scanned in both directions to check for frequency scale asymmetries. No evidence of such asymmetries are observed, which confirms that the laser frequency drift is sufficiently small to ignore.

### A. Experimental linewidth

The experimental linewidth is influenced by both the lasers' bandwidths and the absorption widths of the states under investigation. Fleming and Mooradian [21] studied the spectral properties of external-cavity diode lasers and found bandwidths below 1 MHz. To confirm this result, we used a 1.5 GHz Fàbry-Perot Etalon to place an upper limit on the bandwidth of our external cavities. The etalon's finesse of  $170 \pm 30$  corresponds to a  $9 \pm 2$  MHz instrumental bandwidth. The measured laser linewidth of  $9.7 \pm 0.5$  MHz is clearly limited by the etalon, so the external cavities do not appear to have bandwidths significantly greater than those reported by Fleming and Mooradian.

The natural linewidth for two-photon absorption in an atomic vapor depends on the relative orientation and the detuning of the two laser beams. Bjorkholm and Liao [22] demonstrated that for co-propagating laser beams resonant with an intermediate states, the full width half maximum linewidth is given by

$$\Delta\nu_d + \left| \frac{\nu_1 + \nu_2}{\nu_{s \rightarrow d}} \right| \Delta\nu_p, \quad (2)$$

where  $\Delta\nu_p$  and  $\Delta\nu_d$  are the individual natural widths of the intermediate and final states,  $\nu_{s \rightarrow d}$  is the combined ground-to-final-state transition frequency, and  $\nu_1$  and  $\nu_2$  are the two laser frequencies. Using the 5.2 MHz natural width of the  $6p^2P_{3/2}$  state [23] and the 3.1 MHz natural width of the  $6d^2D_J$  states [3], Eq. (2) predicts a two-photon linewidth of 13 MHz.

Our two laser beams are not exactly co-propagating, but cross within the vapor cell at a shallow angle (4.5 mrad). The most notable consequence of this finite crossing angle is that a small component of the vapor's Doppler profile is sampled. The absorption profile of an individual  $6p^2P_{3/2}(F')$  hyperfine level in a room temperature vapor is Doppler-broadened to about 400 MHz. With a 4.5 mrad angle between the two laser beams, the residual Doppler profile is about 2 MHz.

Assuming 1 MHz laser bandwidths, a 13 MHz linewidth of the two photon transition, and a 2 MHz Doppler width,

the observed linewidth should be approximately 15 MHz. We observe linewidths in the range of 15 MHz to 25 MHz with the extreme  $F$ -states having the narrowest linewidths. This  $F$ -dependence is characteristic of the broadening caused by optical pumping of the ground state (see Sec. III for actual spectra). The same broadening effect is reported in [3], where it is shown that this broadening is sensitive to the presence of a ground-state repump laser.

Our experimental design minimizes other broadening effects, such as power broadening and collisional broadening. We observe power broadening only at laser intensities above  $4 \text{ mW/cm}^2$ , so we collect data at significantly lower laser intensities ( $80\text{--}400 \mu\text{W/cm}^2$ ).

Collisional broadening is a serious concern because of its influence on hyperfine intervals [24]. We curtail this effect by using vapor cells that are evacuated to  $10^{-7}$  Torr before introducing the cesium vapor. The cesium vapor density is further controlled by enclosing the vapor cells within chilled water jackets, maintaining both cells at  $16^\circ\text{C}$ , where the cesium number density is about  $2 \times 10^{10} \text{ cm}^{-3}$ . Of the various states involved in this experiment, the  $6p^2P_{3/2}$  state of cesium has the highest collisional cross section, which makes it the chief contributor to collisional broadening. Resonance broadening of this state under our experimental conditions should contribute at most a few kilohertz to the overall linewidth [25], which is several orders of magnitude below our level of sensitivity.

### B. Frequency calibration

Accurate frequency calibration is critical for the success of most spectroscopic experiments, the present experiment being no exception. It is common to calibrate laser scans with a Fàbry-Perot etalon that is referenced to a frequency standard. This approach requires exacting mechanical and thermal stability to achieve high precision, and laser scans of only a few hundred megahertz require long etalons, on the order of one meter.

We developed a RF modulation technique that is more suitable to our scan lengths and which circumvents mechanical and thermal stability demands by taking advantage of the inherent stability of an atomic frequency standard. We use a rubidium frequency standard (SRS, Model PRS10), which is referenced to the  $^{87}\text{Rb } 5s^2S_{1/2}(F=1) \leftrightarrow 5s^2S_{1/2}(F=2)$  ground hyperfine transition at 6,834,682,612.8 Hz [1]. This frequency standard offers both short-term stability ( $2 \times 10^{-11} \Delta\nu/\nu$  per second) and long-term accuracy ( $5 \times 10^{-10} \Delta\nu/\nu$  per year).

A RF signal generator (Marconi Instruments, model 2024), with a 1 Hz resolution, is locked to the rubidium frequency standard. The RF signal generator drives an EOM at 30–190 MHz, producing frequency sidebands. As the laser is scanned, atomic spectral features appear at precise intervals equal to the modulation frequency. The frequency scale is calibrated using the known value of these intervals. Since two first-order sidebands are produced by phase modulation, we are able to evaluate as well as compensate for the non-linearity of the laser scan.

## III. RESULTS AND DATA ANALYSIS

Typical absorption spectra for the  $6d^2D_{5/2}$  and  $6d^2D_{3/2}$  states are displayed in Figs. 3 and 4. We used nonlinear curve

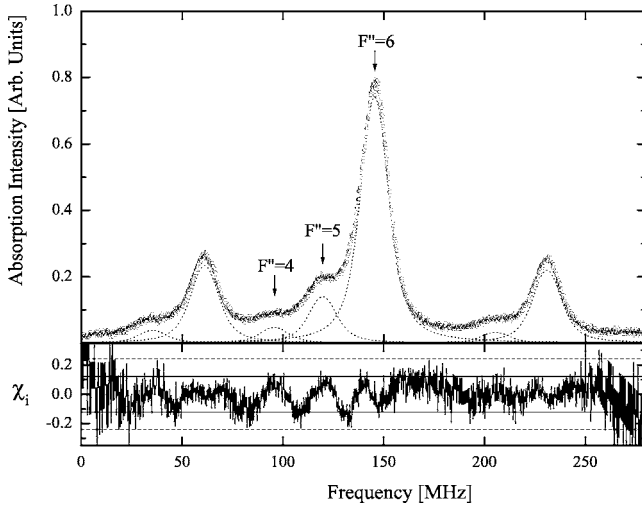


FIG. 3. Absorption spectrum of the  $6p^2P_{3/2}$  ( $F'=5$ )  $\rightarrow 6d^2D_{5/2}$  ( $F''=4,5,6$ ) transition with modulation sidebands at 85 MHz (circles). Also shown are the fitted Voigt profiles (dotted lines). The data are shifted with respect to the Voigt profiles by 3% of the full scale so that both are visible. Plotted on the lower scale are the residuals,  $\chi_i=(y_i-\bar{y}_i)/y_i^{1/2}$ , along with the 68% confidence limit (solid lines) and the 95% confidence limit (dashed lines).

fitting to enhance our resolution and to resolve some of the more closely spaced peaks in the  $6d^2D_{5/2}$  manifold. Using a Levenburg-Marquardt algorithm to minimize the residual, we fit a linear function to the baseline and Voigt profiles to each absorption peak. Each Voigt peak has four fit parameters corresponding to the amplitude, the centroid, the Gaussian width, and the Lorentzian width. The statistical uncertainties for the amplitude and the width parameters are between 0.5% and 5%, while the centroids have statistical

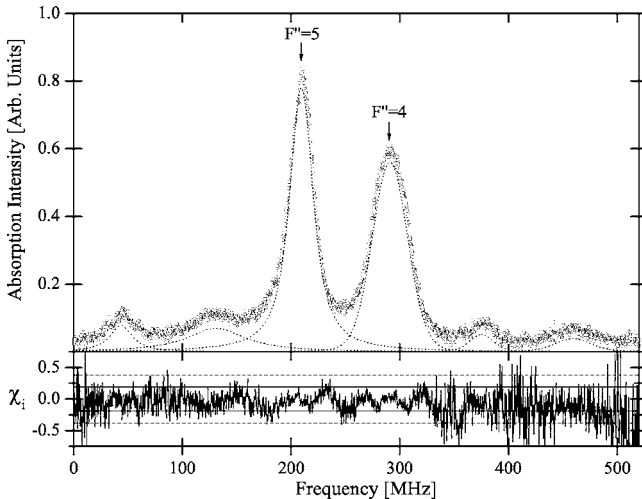


FIG. 4. Absorption spectrum of the  $6p^2P_{3/2}$  ( $F'=5$ )  $\rightarrow 6d^2D_{3/2}$  ( $F''=4,5$ ) transition with modulation sidebands at 165 MHz (circles). Also shown are fitted Voigt profiles (dotted lines). The data are shifted with respect to the Voigt profiles by 2% of the full scale so that both are visible. Plotted on the lower scale are the residuals,  $\chi_i=(y_i-\bar{y}_i)/y_i^{1/2}$ , along with the 68% confidence limit (solid lines) and the 95% confidence limit (dashed lines).

TABLE I. Hyperfine intervals of the  $6d^2D_{5/2}$  state.

Hyperfine interval	This work (MHz)	Ref. [2] (MHz)
$F''=6 \rightarrow F''=5$	$27.5 \pm 0.1$	$29.1 \pm 0.5$
$F''=5 \rightarrow F''=4$	$23.1 \pm 0.2$	$22.1 \pm 0.7$
$F''=4 \rightarrow F''=3$	$18.5 \pm 0.2$	
$F''=3 \rightarrow F''=2$	$14.8 \pm 0.2$	
$F''=2 \rightarrow F''=1$	$9.4 \pm 0.2$	

uncertainties ranging from 10 kHz to 50 kHz.

In addition to data, Figs. 3 and 4 also display the fitted Voigt profiles and the residual for each data point,  $\chi_i$ . Here,  $\chi_i$  is defined as  $(y_i-\bar{y}_i)/y_i^{1/2}$ , where  $y_i$  is the value of the  $i$ th data point and  $\bar{y}_i$  is the corresponding value of the fitted model. We assume that the uncertainty scales with the square root of the signal level. The 68% confidence limit (one sigma) and the 95% confidence limit (two sigma) are calculated using a normal error integral. These confidence limits show that the residual mostly remains below one sigma and does not stray much further than two sigma in the vicinity near the spectral peaks.

The reduced chi-squared parameter  $\chi^2$  is the sum of  $\chi_i^2$  over all data points divided by the degrees of freedom. This parameter ranges between 0.05 and 0.5, indicating good agreement between the model and the data. There is some systematic dispersion of  $\chi_i$  near the centers of the main data points in Figs. 3 and 4. These residuals are, however, fairly symmetric about the peak centers. For example, one can compare the reduced  $\chi^2$  for the left half of any peak to the reduced  $\chi^2$  for the right half of the same peak. In every case, the difference between these  $\chi^2$  values are at least an order of magnitude small than the reduced  $\chi^2$  for the overall spectrum.

As an added measure of the goodness of the fit, we analyzed each spectrum with a stabilized probability plot that rescales the residual using an arctangent-square-root transformation [26]. The stabilized probability shows that all data points within each spectrum fall within the 95% critical limit. This implies normal error distribution and good agreement between each data set and the model.

The frequency scale of each spectrum is calibrated by using the separation between the central absorption peaks and the corresponding modulation sideband (the modulation sidebands are visible in Figs. 3 and 4). Two calibration factors are calculated for each absorption feature: one for the sideband on the high frequency side, and one for the sideband on the low frequency side. The two calibration factors are fitted to a first-order function to estimate the linearity of the laser scan.

Each hyperfine interval is averaged over 40–60 individual spectra. Tables I and II list the resulting hyperfine intervals along with intervals reported previously in the literature. Each uncertainty that we quote is a quadrature combination of the statistical uncertainty (which are standard deviations chiefly due to run-to-run jitter of the peak centroids), the centroid uncertainty produced by the fitting algorithm, and the uncertainty arising from the frequency-scale calibration technique.

TABLE II. Hyperfine intervals of the  $6d^2D_{3/2}$  state.

Hyperfine Interval	This work (MHz)	Ref. [2] (MHz)
$F''=4 \rightarrow F''=5$	$81.8 \pm 0.1$	$81.5 \pm 0.8$
$F''=3 \rightarrow F''=4$	$65.1 \pm 0.2$	
$F''=2 \rightarrow F''=3$	$49.0 \pm 0.1$	

Table II shows good agreement between our work and that of Fort *et al.* [2] for the  $6d^2D_{3/2}$  state, but the  $6d^2D_{5/2}$  state compares less favorably. Our measurements of the  $6d^2D_{5/2}$  manifold, however, are consistent with the hyperfine coupling constants reported by Ref. [3] (see below), whereas the  $6d^2D_{5/2}$  intervals reported by Fort *et al.* are not compatible with Ref. [3]. This disagreement may be due to complications that Fort *et al.* encountered from the Autler-Townes effect in their spectra arising from the relatively intense trapping light present in their experimental arrangement. The Autler-Townes splittings make careful analysis of the closely spaced  $6d^2D_{5/2}$  state particularly difficult.

We generate the hyperfine coupling constants by applying Eq. (1) to the hyperfine intervals from Tables I and II. The result is a set of coupled linear equations. For  $I=\frac{7}{2}$  and  $J=\frac{5}{2}$ , Eq. (1) becomes:

$$\begin{aligned}
6A + \frac{18}{35}B &= -27.5 \pm 0.1 \text{ MHz}, \\
5A + \frac{1}{28}B &= -23.1 \pm 0.2 \text{ MHz}, \\
4A - \frac{8}{35}B &= -18.5 \pm 0.2 \text{ MHz}, \\
3A - \frac{9}{28}B &= -14.8 \pm 0.2 \text{ MHz}, \\
2A - \frac{2}{7}B &= -9.4 \pm 0.2 \text{ MHz},
\end{aligned} \tag{3}$$

and for  $J=\frac{3}{2}$ , Eq. (1) becomes:

$$\begin{aligned}
5A + \frac{5}{7}B &= 81.8 \pm 0.1 \text{ MHz}, \\
4A - \frac{2}{7}B &= 65.1 \pm 0.2 \text{ MHz}, \\
3A - \frac{5}{7}B &= 49.0 \pm 0.1 \text{ MHz},
\end{aligned} \tag{4}$$

where the right-hand side of both sets of coupled equations are the measured splittings. The negative splittings in Eq. (3) represent the inverted nature of the  $6d^2D_{5/2}$  hyperfine manifold (see Fig. 1). Using the method of least squares, we determine the magnetic dipole coupling constant  $A$  and the

TABLE III. The magnetic dipole ( $A$ ) and electric quadrupole ( $B$ ) coupling constants of the  $6d^2D_{5/2}$  state and the  $6d^2D_{3/2}$  state.

Hyperfine manifold	$A$ (MHz)	$B$ (MHz)
$6d^2D_{5/2}$	$-4.66 \pm 0.04^a$ $-4.69 \pm 0.04^b$ $-3.6 \pm 1.0^c$	$0.9 \pm 0.8^a$ $0.18 \pm 0.73^b$
$6d^2D_{3/2}$	$16.34 \pm 0.03^a$ $16.30 \pm 0.15^c$	$-0.1 \pm 0.2^a$ $< \pm 8^c$

<sup>a</sup>Present work.

<sup>b</sup>Reference [3].

<sup>c</sup>Reference [19].

electric quadrupole coupling constant  $B$ , and we propagate the uncertainties through these formulas. The results are reported in Table III, along with the coupling constants obtained by Georgiades *et al.* [3] and Tai *et al.* [19].

Our results for the  $6d^2D_{5/2}$  state are within one standard deviation of those of Refs. [3,19]. Our experimental approach is similar to that of Georgiades *et al.*, but also differs significantly. Both use two-photon optical spectroscopy and rely on a modulation technique for frequency calibration. However, Georgiades *et al.* use nonresonant multiphoton excitation rather than resonantly enhanced excitation, and their atomic sample is contained within a magneto-optical trap. Also, their calibration method is considerably different. Significant advantages of the approach of Ref. [3] include the inherently narrow linewidths of the cold trapped sample and the presence of the repump laser which suppresses broadening caused by optical pumping. The chief disadvantage is that the trap only contains cesium atoms in the  $6s^2S_{1/2}(F=4)$  state, rendering the  $6d^2D_{5/2}(F''=1)$  state not observable, therefore providing only four of the five hyperfine intervals. Our experimental approach accesses all six hyperfine sublevels and measure all five hyperfine intervals.

For the  $6d^2D_{3/2}$  state, our results also agree with that of Tai *et al.* [19], who used cascade-radio-frequency spectroscopy to measure the relevant coupling constants. Our resonant two-photon approach eliminates the strong magnetic field required in cascade-radio-frequency spectroscopy. We significantly improved upon the precision of Tai *et al.*, reducing the uncertainty of  $A$  by a factor of 5 and improving the constraints on  $B$  by nearly two orders of magnitude.

#### IV. CONCLUSION

We measure the hyperfine splittings of the  $6d^2D_{5/2}$  and  $6d^2D_{3/2}$  states of  $^{133}\text{Cs}$  in a low-pressure vapor cell using resonant two-photon, sub-Doppler, absorption spectroscopy. We use all five hyperfine intervals to calculate the hyperfine coupling constants for the  $6d^2D_{5/2}$  state ( $A = -4.66 \pm 0.04$  MHz,  $B = 0.9 \pm 0.8$  MHz), agreeing with previous measurements [3,19], and confirming the accuracy of our experimental approach. We also measure the hyperfine splittings of the  $6d^2D_{3/2}$  state and generate hyperfine coupling constants ( $A = 16.34 \pm 0.03$  MHz,  $B = -0.09 \pm 0.31$  MHz),

which agree with, but significantly improve upon the precision of values previously reported in the literature [19].

#### ACKNOWLEDGMENTS

We express our gratitude to Richard Mertz, Physics Department Technician at Lafayette College, for his assistance in fabricating the apparatus used in this investigation. Associate Professor Duncan Tate of Colby College substantially aided in the design of the external-cavity lasers and provided

important advice concerning the interpretation of our results and the writing of this article. Associate Professor William Jamison of Lafayette College provided equipment and invaluable guidance with the design of the radio-frequency instrumentation. Professor John Huennekens of Lehigh University contributed essential advice and encouragement for writing this article. This work is generously supported through grants provided by Lafayette College and by a National Science Foundation Grant No. PHY-0244684.

- 
- [1] E. Arimondo, M. Inguscio, and P. Violino, *Rev. Mod. Phys.* **49**, 31 (1977).
- [2] C. Fort, F. S. Cataliotti, P. Raspollini, G. M. Tino, and M. Inguscio, *Z. Phys. D: At., Mol. Clusters* **34**, 91 (1995).
- [3] N. Ph. Georgiades, E. S. Polzik, and H. J. Kimble, *Opt. Lett.* **19**, 1474 (1994).
- [4] R. J. Rafac and C. E. Tanner, *Phys. Rev. A* **56**, 1027 (1997).
- [5] W. Yei, A. Sieradzan, E. Cerasuolo, and M. D. Havey, *Phys. Rev. A* **57**, 3419 (1998).
- [6] Th. Udem, J. Reichert, T. W. Hänsch, and M. Kourogi, *Phys. Rev. A* **62**, 031801(R) (2000).
- [7] V. Gerginov, A. Derevianko, and C. E. Tanner, *Phys. Rev. Lett.* **91**, 072501 (2003).
- [8] M. S. Safronova, W. R. Johnson, and A. Derevianko, *Phys. Rev. A* **60**, 4476 (1999).
- [9] V. A. Dzuba, V. V. Flambaum, and J. S. M. Ginges, *Phys. Rev. A* **63**, 062101 (2001).
- [10] C. S. Wood, S. C. Bennet, D. Cho, B. P. Masterson, J. L. Roberts, C. E. Tanner, and C. E. Wieman, *Science* **275**, 1759 (1997).
- [11] J. Guéna, M. Lintz, and M. A. Bouchiat, *Phys. Rev. A* **71**, 042108 (2005).
- [12] M. G. Kozlov, S. G. Porsev, and I. I. Tupitsyn, *Phys. Rev. Lett.* **86**, 3260 (2001).
- [13] B. K. Sahoo, G. Gopakumar, R. K. Chaudhuri, B. P. Das, H. Merlitz, U. S. Mahapatra, and D. Mukherjee, *Phys. Rev. A* **68**, 040501(R) (2003).
- [14] S. J. Pollock and M. C. Welliver, *Phys. Lett. B* **464**, 177 (1999).
- [15] M. C. Welliver and S. J. Pollock, *Phys. Lett. B* **551**, 86 (2003).
- [16] T. W. Koeber, M. Schacht, W. Nagourney, and E. N. Fortson, *J. Phys. B* **36**, 637 (2003).
- [17] M. S. Safronova and C. W. Clark, *Phys. Rev. A* **69**, 040501(R) (2004).
- [18] G. K. Woodgate, *Elementary Atomic Structure*, 2nd ed. (Oxford University Press, Oxford, 1980).
- [19] C. Tai, W. Happer, and R. Gupta, *Phys. Rev. A* **12**, 736 (1975).
- [20] K. B. MacAdam, A. Steinbach, and C. Wieman, *Am. J. Phys.* **60**, 1098 (1992).
- [21] M. W. Fleming and A. Mooradian, *IEEE J. Quantum Electron.* **17**, 44 (1981).
- [22] J. E. Bjorkholm and P. F. Liao, *Phys. Rev. A* **14**, 751 (1976).
- [23] R. J. Rafac, C. E. Tanner, A. E. Livingston, and H. G. Berry, *Phys. Rev. A* **60**, 3648 (1999).
- [24] N. Allard and J. Kielkopf, *Rev. Mod. Phys.* **54**, 1103 (1982).
- [25] Z. J. Jabbour, J. Sagle, R. K. Namiotka, and J. Huennekens, *J. Quant. Spectrosc. Radiat. Transf.* **54**, 767 (1995).
- [26] John R. Michael, *Biometrika* **70**, 11 (1983).